

VIRIAL MASSES AND THE BARYON FRACTION IN GALAXIES[†]

H. HOEKSTRA^{1,2,3}, B.C. HSIEH^{4,5}, H.K.C. YEE³, H. LIN⁶, M.D. GLADDERS⁷

Draft version February 5, 2008

ABSTRACT

We have measured the weak lensing signal as a function of restframe B , V , and R -band luminosity for a sample of ‘isolated’ galaxies. These results are based on four-band photometry from the Red-Sequence Cluster Survey, enabling us to determine photometric redshifts for a large number of galaxies. We select a secure sample of lenses with photometric redshifts $0.2 < z < 0.4$ and study the relation between the virial mass and baryonic contents. In addition, we discuss the implications of the derived photometric redshift distribution for published cosmic shear studies. The virial masses are derived from a fit to the observed lensing signal. For a galaxy with a fiducial luminosity of $10^{10} h^{-2} L_{B\odot}$ we obtain a mass $M_{\text{vir}} = 9.9^{+1.5}_{-1.3} \times 10^{11} M_{\odot}$. The virial mass as a function of luminosity is consistent with a power-law $\propto L^{1.5}$, with similar slopes for the three filters considered here. These findings are in excellent agreement with results from the Sloan Digital Sky Survey and semi-analytic models of galaxy formation. We measure the fraction of mass in stars and the baryon fraction in galaxies by comparing the virial mass-to-light ratio to predicted stellar mass-to-light ratios. We find that star formation is inefficient in converting baryons into stars, with late-type galaxies converting $\sim 33\%$ and early-type galaxies converting only $\sim 14\%$ of baryons into stars. Our results imply that the progenitors of early-type galaxies must have low stellar mass fractions, suggestive of a high formation redshift.

Subject headings: cosmology: observations — dark matter — gravitational lensing — galaxies: haloes

1. INTRODUCTION

Observations of rotation curves of spiral galaxies and measurements of the velocity dispersions of stars in early-type galaxies have provided important evidence for the existence of massive dark matter halos around galaxies (e.g., van Albada & Sancisi 1986). In addition, these studies have presented evidence of tight relations between the baryonic and dark matter components (e.g., Tully & Fisher 1977; Faber & Jackson 1976). Results based on strong lensing by galaxies support these findings (e.g., Keeton, Kochanek & Falco 1998).

The origin of these scaling relations must be closely related to the process of galaxy formation, but the details are still not well understood, mainly because of the complex behaviour of the baryons. Furthermore, on the small scales where baryons play such an important role, the accuracy of cosmological numerical simulations is limited. This complicates a direct comparison of models of galaxy formation to observational data. For such applications, it would be more convenient to have observational constraints on quantities that are robust and easily extracted

from numerical simulations.

An obvious choice is the virial mass of the galaxy, but most techniques for measuring mass require visible tracers of the potential, confining the measurements to relatively small radii. Fortunately, recent developments in weak gravitational lensing have made it possible to probe the ensemble averaged mass distribution around galaxies out to large projected distances. The tidal gravitational field of the dark matter halo introduces small coherent distortions in the images of distant background galaxies, which can be easily detected in current large imaging surveys. We note that one can only study ensemble averaged properties, because the weak lensing signal induced by an individual galaxy is too small to be detected.

Since the first detection of this so-called galaxy-galaxy lensing signal by Brainerd et al. (1996), the significance of the measurements has improved dramatically, thanks to new wide field CCD cameras on a number of mostly 4m class telescopes. This has allowed various groups to image large areas of the sky, yielding the large numbers of lenses and sources needed to measure the lensing signal. For instance, Hoekstra et al. (2004) used 45.5 deg^2 of R_C -band imaging data from the Red-Sequence Cluster Survey (RCS), enabling them to measure, for the first time, the extent and flattening of galaxy dark matter halos, providing strong support for the cold dark matter (CDM) paradigm. However, the analysis presented in Hoekstra et al. (2004) was based on the R_C -band data alone, and consequently lacked redshift information for the individual lenses.

An obvious improvement is to obtain redshift information for the lenses (and if possible the sources). This allows one to study the lensing signal as a function of lens properties, most notably the luminosity. Photometric redshifts were used by Hudson et al. (1998) to scale the lensing signal of galaxies in the Hubble Deep Field,

[†] Based on observations from the Canada-France-Hawaii Telescope, which is operated by the National Research Council of Canada, le Centre National de la Recherche Scientifique and the University of Hawaii.

¹ Department of Physics and Astronomy, University of Victoria, Victoria, BC, V8P 5C2, Canada

² CITA, University of Toronto, Toronto, Ontario M5S 3H8, Canada

³ Department of Astronomy & Astrophysics, University of Toronto, 60 St. George Street, Toronto, Ontario M5S 3H8, Canada

⁴ Institute of Astronomy, National Central University, No. 300, Jhongda Rd. Jhongli City, Taoyuan County 320, Taiwan, R.O.C.

⁵ Institute of Astrophysics & Astronomy, Academia Sinica, P.O. Box 23-141, Taipei 106, Taiwan, R.O.C

⁶ Fermi National Accelerator Laboratory, P.O. Box 500, Batavia, IL 60510

⁷ Carnegie Observatories, Pasadena, CA 91101, USA

and by Wilson et al. (2001) who measured the lensing signal around early-type galaxies as a function of redshift. Smith et al. (2001) and Hoekstra et al. (2003) used spectroscopic redshifts, but the lens samples involved were rather small (~ 1000). The Sloan Digital Sky Survey (SDSS) combines both survey area and redshift information. Its usefulness for galaxy-galaxy lensing was demonstrated clearly by Fischer et al. (2000). More recently, McKay et al. (2001) used the available SDSS redshift information to study the galaxy-galaxy lensing signal as a function of galaxy properties (also see Guzik & Seljak 2002; Seljak 2002; Sheldon et al. 2004).

In this paper we use a subset of the RCS data, for which photometric redshifts have been determined using B, V, R_C and z' data taken using the Canada-France-Hawaii Telescope (see Hsieh et al. 2005 for details). The area covered by these multiwavelength data is approximately 33.6 deg^2 , resulting in a catalog of 1.2×10^6 galaxies for which a redshift could be determined, making it one of the largest data sets of its kind. This unique data set allows us to measure the virial masses of galaxies as a function of their luminosity.

This paper is structured as follows. In §2 we briefly discuss the data, including the photometric redshift catalog and its accuracy. The results of some basic tests of the photometric redshifts are presented in §3. In §4 we discuss the dark matter profile inferred from numerical simulations. The measurement of the virial mass as a function of luminosity in various filters is presented in §5, as well as our measurement of the baryon fraction in galaxies. Throughout the paper we adopt a flat cosmology with $\Omega_m = 0.3$, $\Omega_\Lambda = 0.7$ and a Hubble parameter $H_0 = 100h \text{ km/s/Mpc}$.

2. DATA

The Red-Sequence Cluster Survey (RCS) is a galaxy cluster survey designed to provide a large sample of optically selected clusters of galaxies in a large volume (see Gladders & Yee (2005) for a detailed discussion of the survey). To this end, 92 deg^2 of the sky were imaged in both R_C and z' using the CFH12k camera on CFHT and the Mosaic II camera on the CTIO Blanco telescope. This choice of filters allows for the detection of clusters up to $z \sim 1.4$ using the cluster red-sequence method developed by Gladders & Yee (2000).

After completion of the original RCS survey, part of the surveyed area was imaged in both B and V band using the CFHT. This additional color information allows for a better selection of clusters at lower redshifts. These follow-up observations cover $\sim 33.6 \text{ deg}^2$, thus covering $\sim 70\%$ of the CFHT fields. The data and the photometric reduction are described in detail in Hsieh et al. (2005).

The galaxy-galaxy lensing results presented in Hoekstra et al. (2004) were based on 45.5 deg^2 of R_C -band data alone. The addition of B and V imaging data for 33.6 deg^2 to the existing R_C and z' data allow for the determination of photometric redshifts for both lenses and sources in this subset of RCS imaging data. This enables the study of the lensing signal as a function of the photometric properties of the lens galaxies (i.e., color and luminosity). In this paper we focus on this multi-color subset of the RCS.

To determine the restframe B , V and R luminosities we use template spectra for a range in spectral types

and compute the corresponding passband corrections as a function of redshift and galaxy color (this procedure is similar to the one described in van Dokkum & Franx 1996). Provided the observed filters straddle the redshifted filter of interest, which is the case here, this procedure yields very accurate corrections.

The CFHT R_C images are used to measure the shapes of galaxies used in the weak lensing analysis. The raw galaxy shapes are corrected for the effects of the point spread function, as described in Hoekstra et al. (2002a). The resulting object catalogs have been used for a range of weak lensing studies (e.g., Hoekstra et al. 2002a, 2002b, 2002c, 2004) and we refer to these papers for a detailed discussion of the shape measurements.

The measurements of the lensing signal caused by large scale structure presented in Hoekstra et al. (2002a, 2002b) are very sensitive to residual systematics. The various tests described in these papers suggest that the systematics are well under control. In this paper we use the shape measurements to measure the galaxy-galaxy lensing signal, which is much less sensitive to these observational distortions: in galaxy-galaxy lensing one measures the lensing signal that is perpendicular to the lines connecting many lens-source pairs. These are randomly oriented with respect to the PSF anisotropy, and therefore residual systematics are suppressed.

2.1. Photometric redshift distribution

The determination of the photometric redshifts is described in detail in Hsieh et al. (2005). The empirical quadratic polynomial fitting technique (Connolly et al. 1995) is used to estimate redshifts for the galaxies in the RCS data. The key component in this approach is the creation of a training set. Spectroscopic redshifts from the CNOC2 survey (Yee et al. 2000) are matched to the corresponding objects in the overlapping RCS fields. These data are augmented with observations of the GOODS/HDF-N field, for which the spectroscopic redshifts have been obtained using the Keck telescope (Wirth et al. 2004; Cowie et al. 2004), and the photometry is from the ground-based Hawai'i HDF-N data obtained with the Subaru telescope (Capak et al. 2004). This results in a final training set that includes 4,924 objects covering a large range in redshifts. To minimize the fitting errors arising from different galaxy types, Hsieh et al. (2005) used a kd-tree method with 32 cells in a three-dimensional color-color-magnitude space.

The resulting catalog contains 1.2×10^6 galaxies with photometric redshifts. This catalog was matched against the catalog of galaxies for which shapes were measured. This resulted in a sample of 8×10^5 galaxies with $18 < R_C < 24$, that are used in the analysis presented here.

Comparison with the spectroscopic redshifts shows that accurate photometric redshifts, with $\sigma_z < 0.06$, can be derived in the range $0.2 < z < 0.5$. At lower redshifts, the lack of U band data limits the accuracy, whereas at higher redshifts photometric errors increase the scatter to $\sigma_z \sim 0.12$ (see Hsieh et al. 2005 for more details).

To study the halos of galaxies as a function of color and luminosity we select a sample of lenses at intermediate redshifts: we select galaxies with photometric redshifts $0.2 < z < 0.4$ and R_C -band magnitudes $18 < R_C < 24$. This redshift range is well covered by the CNOC2 redshift survey at the bright end, and the redshift errors

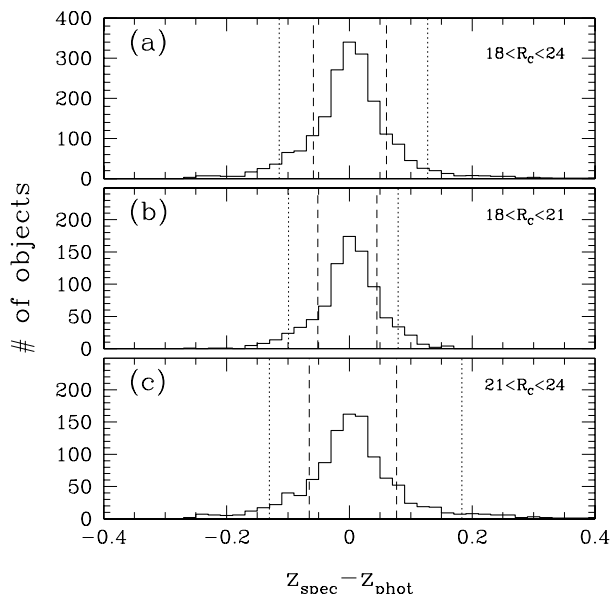


FIG. 1.— *panel a*: The difference in spectroscopic and photometric redshifts for galaxies in the training set, with $18 < R < 24$ and photometric redshifts $0.2 < z_{\text{phot}} < 0.4$. Our sample of lenses is selected to be in this redshift and magnitude range. The dotted lines indicate the intervals containing 90% of the galaxies and the dashed lines indicate the 70% interval. *panel b*: Same, but now for the brighter half of the training set, i.e., galaxies with $18 < R < 21$. *panel c*: Same, but for the galaxies with $21 < R < 24$, the fainter half of the lenses.

are relatively small. For the background galaxies we limit the analysis to galaxies with $z_{\text{phot}} < 1$.

Figure 1 shows the difference between spectroscopic and photometric redshifts for different subsets of galaxies with photometric redshifts $0.2 < z < 0.4$. Panel a shows the full sample, whereas panels b and c show the bright and faint halves respectively. The distribution is peaked, with 70% of the galaxies within the range $|\Delta z| < 0.06$ (0.05 and 0.07 for the bright and faint subsets, resp.) and 90% within $|\Delta z| < 0.12$ (0.085 and 0.15 for the bright and faint subsets, resp.).

The solid histogram in Figure 2a shows the normalized photometric redshift distribution for the galaxies brighter than $R_C = 24$. It is common to parametrize the redshift distribution, and a useful form is given by

$$p(z) = \frac{\beta}{z_s \Gamma[(1 + \alpha)/\beta]} \left(\frac{z}{z_s}\right)^\alpha \exp \left[- \left(\frac{z}{z_s}\right)^\beta \right]. \quad (1)$$

We fit this model to the observed redshift distribution. However, the uncertainties in the photometric redshift determinations can be substantial, and as a result the observed distribution is broadened. We use the observed error distribution, assuming a normal distribution, to account for the redshift errors. For the best fit parameterization we find values of $z_s = 0.29$, $\alpha = 2$ (fixed) and $\beta = 1.295$, which yields a mean redshift of $\langle z \rangle = 0.53$. This model redshift distribution (which includes the smoothing by redshift errors) is indicated by the smooth curve in Figure 2a.

In the weak lensing analysis, objects are weighted by the inverse square of the uncertainty in the shear measurement (e.g., see Hoekstra et al. 2000, 2002a). As more distant galaxies are fainter, they tend to have somewhat lower weights and the effective redshift distribution

is changed slightly. The dashed histogram in Figure 2a shows the distribution weighted by the uncertainty in the shape measurement for each redshift bin. The best fit parameterized redshift distribution has parameters $z_s = 0.265$, $\alpha = 2.2$ (fixed) and $\beta = 1.30$, which yields $\langle z \rangle = 0.51$, only slightly lower than the unweighted case.

2.2. Implications for cosmic shear results?

Hoekstra et al. (2002b) presented constraints on the matter density Ω_m and the normalization of the power spectrum σ_8 by comparing cold dark matter predictions to the observed lensing signal caused by large scale structure. The derived value for σ_8 depends critically on the adopted redshift distribution. Hoekstra et al. (2002b) used galaxies with $22 < R_C < 24$ and a redshift distribution given by $z_s = 0.302$, $\alpha = 4.7$ and $\beta = 1.7$, which yields a mean redshift of $\langle z \rangle = 0.59$. These parameters were based on a comparison with redshift distributions determined from the Hubble Deep Fields.

It is useful to examine how these assumptions compare to the RCS photometric redshift distribution for galaxies with $22 < R_C < 24$, as displayed in Figure 2b. The best fit model, indicated by the smooth curve, has parameters $z_s = 0.31$, $\alpha = 3.50$ and $\beta = 1.45$, implying a mean redshift of 0.65, about 10% higher than used by Hoekstra et al. (2002b). It is important to note, however, that the training set lacks a large number of objects beyond $z = 0.8$ and $R_C > 22$. Despite these shortcomings, the mean redshift of sources appears higher than what was used in Hoekstra et al. (2002b), thus suggesting that their value for σ_8 needs to be revised downwards. The suggested change in source redshift could reduce the value for σ_8 from Hoekstra et al. (2002b) by about 8% to $\sigma_8 \sim 0.8$. Unfortunately it is not possible to robustly quantify the size of the revision. We stress that without further work on photometric redshifts for faint, high redshift galaxies, it will be difficult to interpret current and, most importantly, future cosmic shear results.

The galaxy-galaxy lensing signal examined in this paper is much less sensitive to the uncertainty in the redshift distribution of faint, distant galaxies, as most of the signal is caused by lenses at much lower redshifts. As mentioned above, to minimize uncertainties in our results further, we only use background galaxies with redshifts less than 1, and select a sample of lenses with redshift $0.2 < z < 0.4$.

3. TESTING THE PHOTOMETRIC REDSHIFTS

Hsieh et al. (2005) present various tests of the accuracy of the photometric redshifts. Comparison to the available spectroscopic data as well as comparing to other published distributions provides a clear way to quantify the uncertainties. In this section we discuss some additional tests, based on the fact that the amplitude of the lensing signal is a well known function of the source redshift. Such a test provides a useful “sanity” check on the validity of the photometric redshift distribution.

The azimuthally averaged tangential shear $\langle \gamma_t \rangle$ as a function of distance from the lens is a useful measure of the lensing signal (e.g., Miralda-Escudé 1991):

$$\langle \gamma_t \rangle(r) = \frac{\bar{\Sigma}(< r) - \bar{\Sigma}(r)}{\Sigma_{\text{crit}}} = \bar{\kappa}(< r) - \bar{\kappa}(r), \quad (2)$$

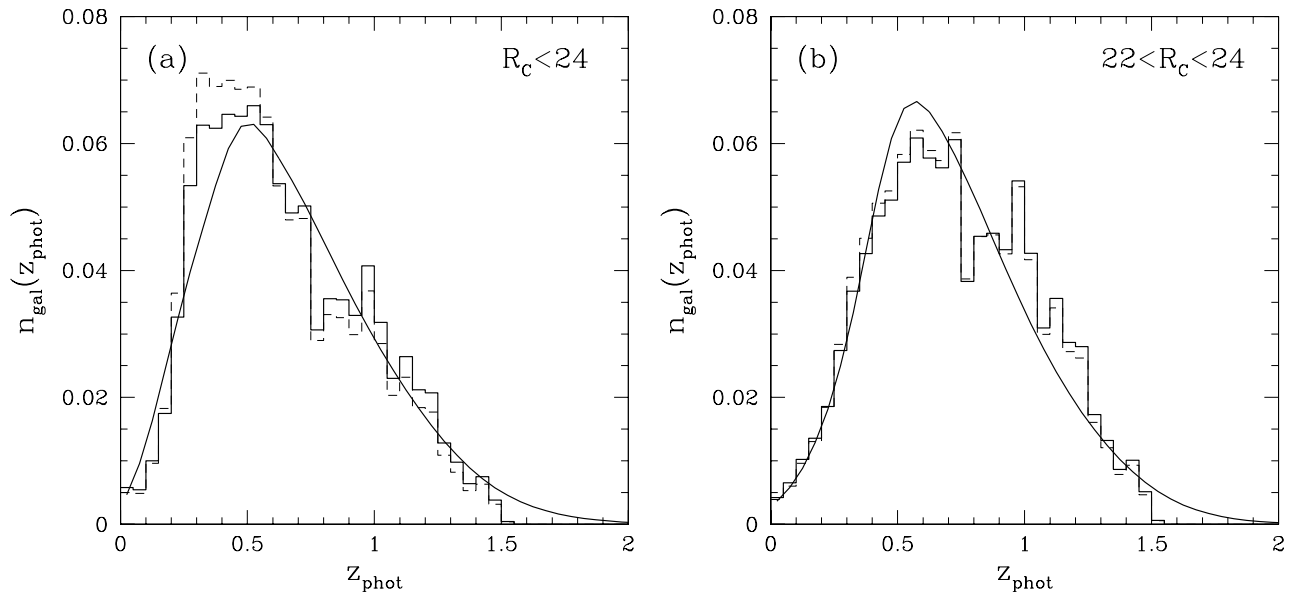


FIG. 2.— *panel a*: The solid histogram shows the normalized photometric redshift distribution for the galaxies with redshifts and magnitudes $R_C < 24$ that are included in the weak lensing analysis. The solid smooth curve shows the best fit model redshift distribution (see text for details). *panel b*: Similar to panel a, but for galaxies with $22 < R_C < 24$, corresponding to the range used by Hoekstra et al. (2002b). It is important to note that the lack of a relatively good training set for $z > 0.6$ limits the interpretation. The dashed histogram shows the distributions weighted by the uncertainty in the shape measurement for each redshift bin.

where $\bar{\Sigma}(< r)$ is the mean surface density within an aperture of radius r , and $\bar{\Sigma}(r)$ is the mean surface density on a circle of radius r . The convergence κ , or dimensionless surface density, is the ratio of the surface density and the critical surface density Σ_{crit} , which is given by

$$\Sigma_{\text{crit}} = \frac{c^2}{4\pi G} \frac{D_s}{D_l D_{ls}}, \quad (3)$$

where D_l is the angular diameter to the lens. D_s and D_{ls} are the angular diameter distances from the observer to the source and from the lens to the source, respectively. It is convenient to define the parameter

$$\beta = \max[0, D_{ls}/D_s], \quad (4)$$

which is a measure of how the amplitude of the lensing signal depends on the redshifts of the source galaxies. For instance, in the case of a singular isothermal sphere (SIS) model, the dimensionless surface density is

$$\kappa = \gamma_t = \frac{r_E}{2r}, \quad (5)$$

where r_E is the Einstein radius. Under the assumption of isotropic orbits and spherical symmetry, the Einstein radius (in radians) is related to the velocity dispersion and β through

$$r_E = 4\pi \left(\frac{\sigma}{c} \right)^2 \beta. \quad (6)$$

To test the photometric redshifts from the RCS, we use galaxies with photometric redshifts $0.2 < z < 0.4$ to define a sample of lenses. We compute the ensemble averaged tangential shear around these galaxies (i.e., the galaxy-mass cross-correlation function) as a function of source redshift. Brighter galaxies are expected to be

more massive, and should be given more weight. To derive the lensing signal, we assume that the velocity dispersion scales with luminosity as $\sigma \propto L_B^{0.3}$, a choice which is motivated by the observed slope of the B -band Tully-Fisher relation (e.g., Verheijen 2001).

We select bins with a width of 0.1 in redshift, and measure the galaxy-mass cross-correlation function (e.g., see Hoekstra et al. 2004; Sheldon et al. 2004) out to 10 arcminutes. This signal arises from the combination of the clustering properties of the lenses and the underlying dark matter distribution. In the remainder of the paper, while studying the properties of dark matter halos around galaxies, we limit the analysis to smaller radii and to ‘isolated’ lenses. However, by extending the range of measurements in this section, the signal-to-noise ratio is higher. The signal is well described by a SIS model for this range of scales (as suggested by the reduced χ^2 values for the fits). The resulting value for the Einstein radius as a function of redshift for the background galaxies is presented in Figure 3.

We find a negligible lensing signal for galaxies at the redshift of the lenses, whereas it increases for more distant sources. For a given cosmology and a pair of lens and source redshifts the value of β can be readily computed. However, the errors in the photometric redshift determination complicate such a simple comparison between the expected signal and the results presented in Figure 3. As was the case for the photometric redshift distribution, the redshift errors will change the signal. For instance at low redshifts, higher redshift galaxies will scatter into this bin, thus increasing the lensing signal. At higher redshifts, lower redshift object will scatter upwards, lowering the signal.

When comparing the observed signal to the signal expected based on the adopted Λ CDM cosmology we need account for these redshift errors. To this end, we cre-

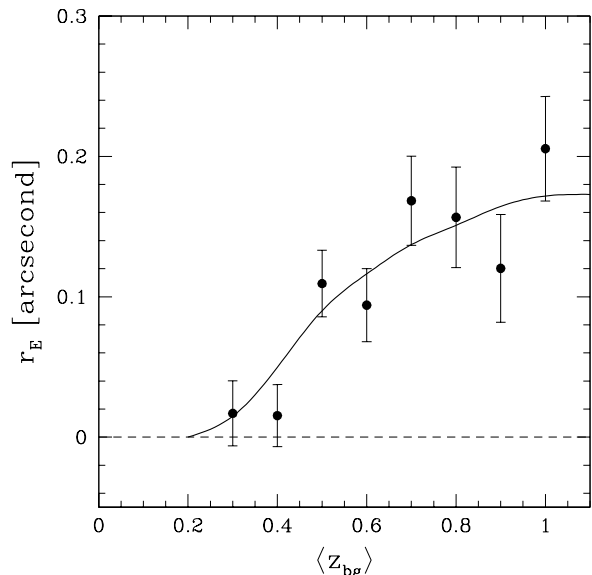


FIG. 3.— Best fit Einstein radius obtained from a fit to the tangential shear as a function of redshift of the background galaxies. Lenses were selected to have photometric redshifts in the range $0.2 < z < 0.4$. The solid line corresponds to the dependence of the lensing signal for a Λ CDM cosmology. The observed lensing signal scales with redshift as expected.

ate simulated catalogs. The first step is to compute a model lensing signal based on the observed photometric redshifts (which are taken to be exact). We then create a mock catalog by adding the random errors to the redshift (while leaving the lensing signal unchanged). These random errors are based on the observed distribution (see e.g., Fig. 1). We measure the lensing signal as a function of redshift in the mock catalog. This signal, indicated by the solid line in Figure 3 can be compared directly to our actual measurements as it now includes the smoothing effect of redshift errors. Figure 3 shows that it traces the observed change in amplitude of the lensing signal very well.

Another useful experiment is to measure the lensing signal when the lenses and sources are in the same redshift bin. We note that this procedure enhances the probability that we measure the signal for galaxies which are physically associated. If satellite galaxies tend to be aligned tangentially (radially) this would also lead to a positive (negative) signal. The results from Bernstein & Norberg (2002), based on an analysis employing spectroscopic redshifts, has shown that intrinsic tangential alignments are negligible. Unfortunately, in our case, the much larger photometric redshift errors (compared to spectroscopic redshifts) effectively suppress this potentially interesting signal. In addition, for the RCS data, the interpretation of the signal requires a large set of spectroscopic redshifts to quantify the contributions of unassociated galaxies in each bin.

Instead, we use these measurements as a test of the photometric redshifts. The results are presented in Figure 4. Panel a shows the results for the tangential shear, whereas Panel b shows the results when the background galaxies are rotated by 45° (which is a measure of systematics). In both cases, we do not observe a significant signal. The lack of a signal in the tangential shear in this case implies that the errors in photometric redshifts

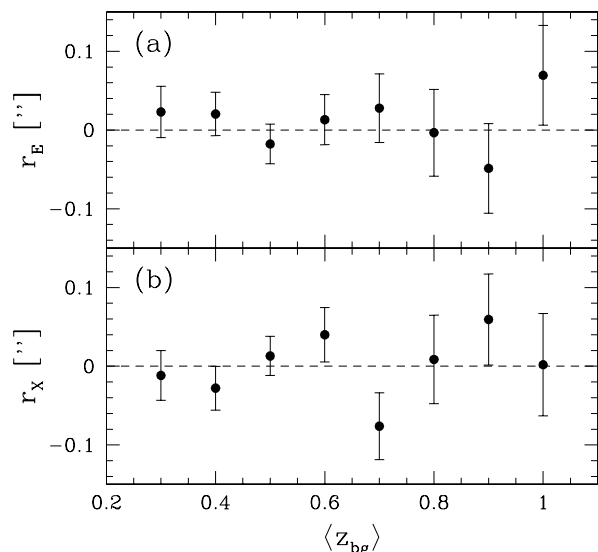


FIG. 4.— *panel a*: Best fit Einstein radius obtained from a fit to the tangential shear when the lenses and sources are selected to be in the same redshift bin. In this case, no signal should be present, in agreement with the measurements. This result also indicates that intrinsic tangential alignments are negligible. *panel b*: Results when the background galaxies are rotated by 45 degrees ('B'-mode). Also in this case no signal is detected.

are relatively small. If this were not the case, and higher redshift galaxies would contaminate the samples at lower redshifts, we would expect to observe a positive signal.

4. GALAXY DARK MATTER PROFILE

One of the major advantages of weak gravitational lensing over dynamical methods is that the lensing signal can be measured out to large projected distances from the lens. However, at large radii, the contribution from a particular galaxy may be small compared to its surroundings: a simple interpretation of the measurements can only be made for 'isolated' galaxies.

In practice, galaxies are not isolated, which is particularly true for bright, early-type galaxies. In their analysis of SDSS data, Guzik & Seljak (2002) quantified the contribution from clustered galaxies using a halo-model approach. As discussed in §5, we follow a different approach by selecting relatively isolated galaxies. As a result, our results are not strictly valid for the galaxy population as a whole. Nevertheless, the selection procedure is well defined and can be readily implemented when comparing to numerical simulations.

We limit the analysis to relatively small distances from the lens, thus ensuring that the signal is dominated by the lens itself. As a result, we need to adopt a model for the mass distribution to relate the lensing signal to the mass of the lens. Our choice is motivated by the results of cold dark matter (CDM) simulations.

Collisionless cold dark matter provides a good description for the observed structures in the universe. Numerical simulations, which provide a powerful way to study the formation of structure in the universe, indicate that on large scales CDM gives rise to a particular density profile (e.g., Dubinski & Carlberg 1991; Navarro, Frenk, & White 1995, 1996, 1997; Moore et al. 1999). We note, however, that there are still uncertainties regarding the

slope at small radii and the best analytical description of the profile (e.g., Moore et al. 1999; Diemand et al. 2004; Hayashi et al. 2004; Tasitsiomi et al. 2004a). Furthermore there is considerable scatter from halo to halo in the simulations. Our observations, however, cannot distinguish between these various profiles, and instead we focus on the commonly used NFW profile, given by

$$\rho(r) = \frac{M_{\text{vir}}}{4\pi f(c)} \frac{1}{r(r+r_s)^2}, \quad (7)$$

where M_{vir} is the virial mass, which is the mass enclosed within the virial radius r_{vir} . The virial radius is related to the ‘scale radius’ r_s through the concentration $c = r_{\text{vir}}/r_s$. The function $f(c) = \ln(1+c) - c/(1+c)$.

One can fit the NFW profile to the measurements with M_{vir} and concentration c (or equivalently r_s) as free parameters. However, numerical simulations have shown that the average concentration depends on the halo mass and the redshift. Hoekstra et al. (2004) constrained the mass and scale radius of the NFW model using a maximum likelihood analysis of the galaxy-galaxy lensing signal, and found that the results agreed well with the predictions from simulations. We therefore adopt the results from Bullock et al. (2001), who found from simulations that

$$c = \frac{9}{1+z} \left(\frac{M_{\text{vir}}}{8.12 \times 10^{12} h M_{\odot}} \right)^{-0.14}. \quad (8)$$

It is good to note that individual halos in the simulations have a lognormal dispersion of approximately 0.14 around the median. For the virial mass estimates presented here, we will use this relation between mass and concentration, thus assuming we can describe the galaxy mass distribution by a single parameter.

By definition, the virial mass and radius are related by

$$M_{\text{vir}} = \frac{4\pi}{3} \Delta_{\text{vir}}(z) \rho_{\text{bg}}(z) r_{\text{vir}}^3, \quad (9)$$

where $\rho_{\text{bg}} = 3H_0^2 \Omega_m (1+z)^3 / (8\pi G)$ is the mean density at the cluster redshift and the virial overdensity $\Delta_{\text{vir}} \approx (18\pi^2 + 82\xi - 39\xi^2)/\Omega(z)$, with $\xi = \Omega(z) - 1$ (Bryan & Norman 1998). For the Λ CDM cosmology considered here, $\Delta_{\text{vir}}(0) = 337$. We also note that for the adopted Λ CDM cosmology the virial mass is different from the widely used M_{200} . This mass is commonly defined as the mass contained within the radius r_{200} , where the mean mass density of the halo is equal to $200\rho_c$ (i.e., setting $\Delta = 200$ and $\rho_{\text{bg}} = \rho_c$ in Eqn. 9). Note, however, that other definitions for M_{200} can be found in the literature as well.

The expressions for the tangential shear and surface density for the NFW profile have been derived by Bartelmann (1996) and Wright & Brainerd (2000) and we refer the interested reader to these papers for the relevant equations.

5. RESULTS

As discussed above, we study a sample of lenses with photometric redshifts $0.2 < z < 0.4$ and $18 < R_C < 24$. This first selection yields $\sim 1.4 \times 10^5$ lenses. We split this sample in a number of luminosity and color bins and determine the virial radii from an NFW model fit to the observed lensing signal.

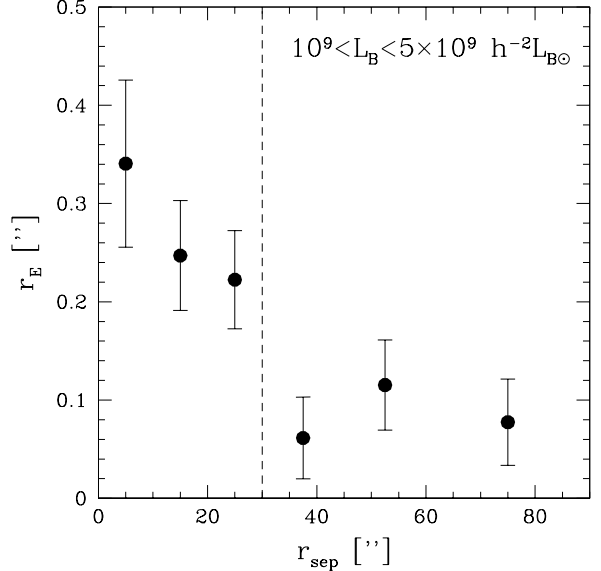


FIG. 5.— Einstein radius for ‘faint’ lenses as a function of projected distance to the nearest ‘bright’ lens r_{sep} . The faint galaxies have luminosities $10^9 < L_B < 5 \times 10^9 h^{-2} L_{B\odot}$, whereas the bright galaxies have $L_B > 5 \times 10^9 h^{-2} L_{B\odot}$.

For bright galaxies the lensing signal on small scales is typically dominated by the dark matter halo associated with that galaxy. In the case of faint (low mass) galaxies, however, the signal can easily be dominated by contributions from a massive neighbor. Note that this neighbor need not be physically associated with the lens, as all matter along the line-of-sight contributes to the lensing signal.

We can study the relevance of the local (projected) density by measuring the lensing signal around a sample of ‘faint’ lenses ($10^9 < L_B < 5 \times 10^9 h^{-2} L_{B\odot}$), as a function of the projected distance to the nearest ‘bright’ lens ($L_B > 5 \times 10^9 h^{-2} L_{B\odot}$). This distance can be used as a crude measure of the density around the faint lens (i.e., the smaller the distance, the higher the density).

To this end, we split this sample of ‘faint’ lenses into subsets based on their distance to the nearest bright galaxy. We fit a SIS model to the ensemble averaged lensing signal out to $2''$ ($\sim 400 h^{-1} \text{kpc}$ at the mean distance of the lenses) for each bin. The reduced χ^2 values for the best fit are all close to unity, indicating that the SIS model provides a good fit to these observations. We found that limiting the fit to smaller radii did not change the results apart from increasing the measurement errors. Figure 5 shows the derived value for the Einstein radius as a function of the distance to the nearest bright galaxy.

The results show a clear increase in lensing signal as the separation decreases, i.e. as the density increases. However, at separations larger than $\sim 30''$, the observed lensing signal appears to be independent of the density. Larger data sets are required to make more definitive statements, but these findings suggest that we can measure the properties of ‘isolated’ faint galaxies by limiting the sample to galaxies which are more than 30 arcseconds away from a brighter galaxy. Although this is a rather strict selection for the faintest galaxies, bright galaxies can be surrounded by many faint galaxies and consequently are not truly isolated. In the remainder of this

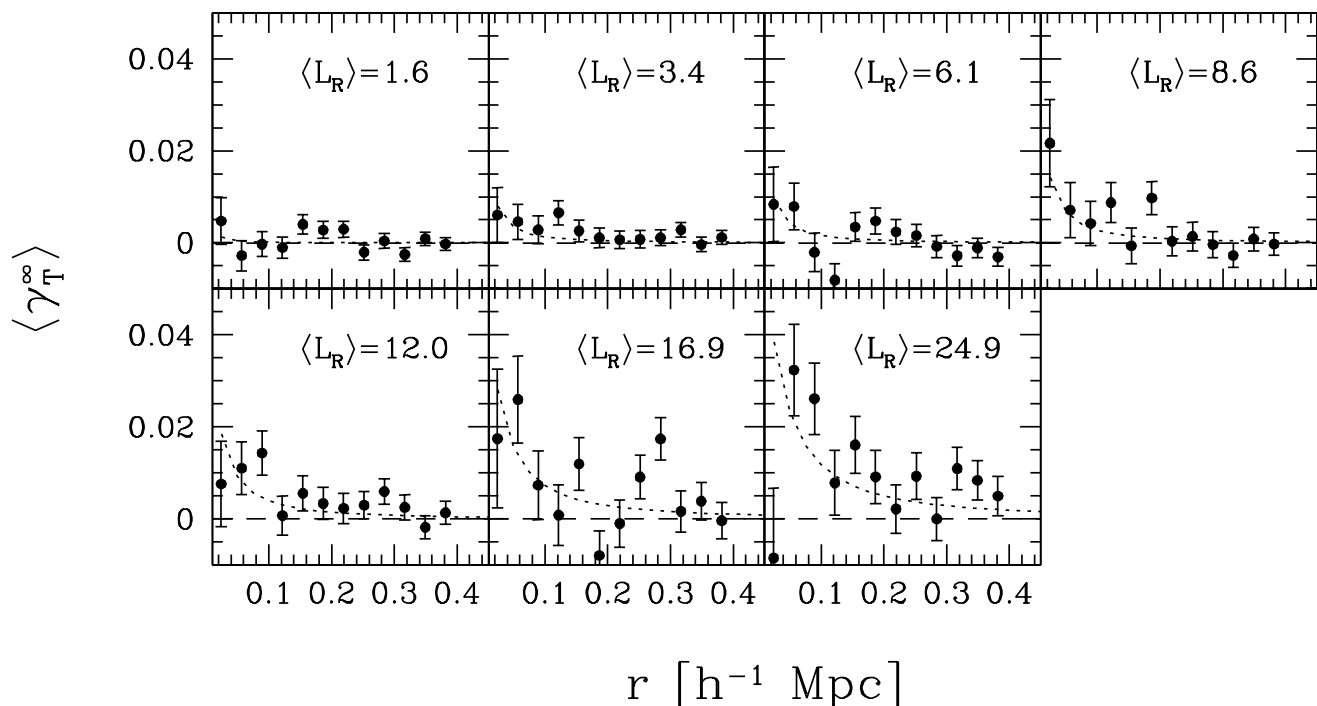


FIG. 6.— Tangential shear as a function of projected (physical) distance from the lens for each of the seven restframe R -band luminosity bins. To account for the fact that the lenses have a range in redshifts, the signal is scaled such that it corresponds to that of a lens at the average lens redshift ($z \sim 0.32$) and a source redshift of infinity. The mean restframe R -band luminosity for each bin is also shown in the figure in units of $10^9 h^{-2} L_{R\odot}$. The strength of the lensing signal clearly increases with increasing luminosity of the lens. The dotted line indicates the best fit NFW model to the data. The tangential shear profiles for the B and V -band are very similar and we only present the final results for the R filter in Figure 8

paper, we present results based on the sample of ‘isolated’ galaxies, unless specified otherwise. This selection reduces the sample of lenses to 94,509 galaxies.

5.1. Mass-luminosity relation

We split the sample of ‘isolated’ lens galaxies into seven luminosity bins and measure the mean tangential distortion as a function of radius out to 2 arcminutes. We fit an NFW profile to these measurements, with the virial mass as a free parameter, as described in §4.

Figure 6 shows the measurements of the tangential shear as a function of projected distance from the lens for the seven R -band luminosity bins. The results for the B and V filters are very similar to the ones presented in Figure 6. To account for the fact that the lenses span a range in redshift, we have scaled the signal such that it corresponds to that of a lens at the mean lens redshift ($z \sim 0.32$) and a background galaxy at infinite redshift. In each panel in Figure 6 the average restframe R -band luminosity for each bin is indicated (in units of $10^9 h^{-2} L_{R\odot}$). The vertical scales in each of the panels in Figure 6 are the same, and as the luminosity of the lenses increases we observe a clear increase in the strength of the lensing signal. The best fit NFW models for each bin are indicated by the dotted curves. Note that the current observations cannot distinguish between an NFW profile (used here) and other profiles such as the SIS model.

There are more faint galaxies relative to the number of bright galaxies and the errors in the photometric redshift estimates will have as the net effect of faint galaxies getting scattered to higher luminosity bins, hence biasing

the mass at fixed luminosity to a lower value. To estimate the level of this bias we create mock catalogs. We assume a power-law mass-luminosity relation and compute the model lensing signal using the observed photometric redshifts of the lens and source galaxies. We analyse this ‘perfect’ catalog and compute the virial masses as a function of luminosity. We then use the observed photometric redshift error distribution as a function of apparent magnitude (see Figure 1) to create a number of new catalogs where the random error is added to the redshift (note that the lensing signal is not changed). These catalogs are also analysed and yield the ‘observed’ virial mass as a function of luminosity.

As expected, the resulting masses are smaller than the input masses and the change in mass depends on the luminosity. The results are presented in Figure 7 for the B , V , and R -band. Different choices for the mass-luminosity relation (within reasonable bounds) yield very similar curves. To infer the correct virial mass, we scale the observed virial masses by these curves.

At the low luminosity end the corrections are large because of the relatively large errors in redshift. At the bright end, however, the redshift errors are smaller, but the number of bright galaxies is decreasing rapidly (because of the shape of the luminosity function), and a relatively larger fraction of intrinsically lower mass systems ends up in the high luminosity bin, resulting in an increase of the correction factor. The corrections are substantial at both ends, but the origin is well understood and the associated uncertainty is small.

The corrected virial masses as a function of luminosity

TABLE 1
BEST FIT VIRIAL MASSES

L_B [$10^9 h^{-2} L_\odot$]	M_{vir} [$10^{11} h^{-1} M_\odot$]	L_V [$10^9 h^{-2} L_\odot$]	M_{vir} [$10^{11} h^{-1} M_\odot$]	L_R [$10^9 h^{-2} L_\odot$]	M_{vir} [$10^{11} h^{-1} M_\odot$]
1.6	$0.66^{+0.41}_{-0.43}$	1.6	$0.48^{+0.33}_{-0.35}$	1.6	$0.10^{+0.40}_{-0.30}$
3.5	$0.86^{+0.42}_{-0.48}$	3.4	$1.05^{+0.69}_{-0.45}$	3.4	$1.24^{+0.65}_{-0.57}$
6.1	$1.81^{+0.84}_{-0.75}$	6.1	$3.1^{+1.2}_{-1.0}$	6.1	$1.62^{+0.88}_{-0.84}$
8.6	$6.0^{+1.6}_{-1.6}$	8.6	$2.6^{+1.3}_{-1.1}$	8.6	$3.1^{+1.4}_{-1.3}$
11.7	$7.7^{+2.0}_{-1.9}$	11.9	$6.6^{+1.9}_{-1.8}$	12.0	$5.0^{+1.5}_{-1.3}$
16.9	$16.9^{+5.5}_{-4.9}$	17.0	$20.1^{+5.3}_{-4.9}$	16.9	$11.5^{+4.0}_{-3.4}$
24.0	$18.8^{+7.8}_{-6.3}$	24.5	$17.2^{+5.6}_{-4.9}$	24.9	$23.3^{+5.6}_{-5.1}$

NOTE. — Best fit virial masses as a function of luminosity in the restframe B , V and R band. The corresponding values for the concentration c can be computed using Eqn. 8 using a redshift of $z = 0.32$ for the lenses. The listed errors indicate the 68% confidence limits.

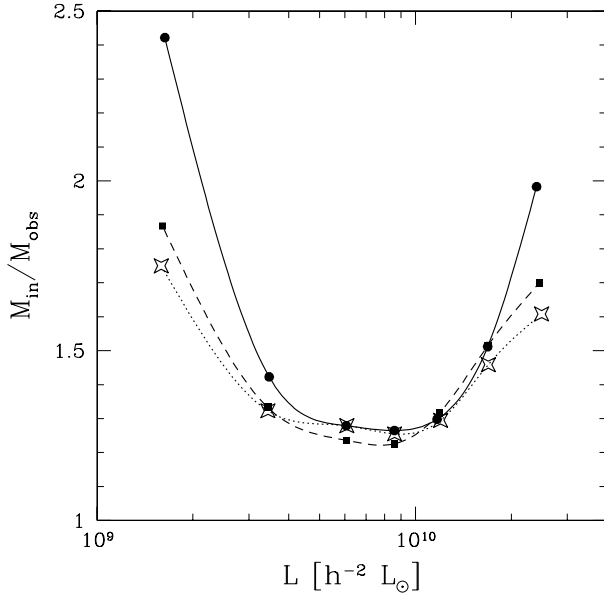


FIG. 7.— The ratio of the input virial mass and the observed mass after adding photometric redshift errors. The dependence with luminosity is dominated by how the redshift errors depend on brightness. The resulting curves depend only very weakly on the input mass-luminosity relation. The corrections are somewhat different for the various restframe bands. The solid line with filled circles correspond to the B -band results, the dashed line with solid squares is for the V -band and the dotted line with stars is for the R -band data. To infer the correct virial mass, we scale the observed virial masses by these curves.

in the B , V , and R -band respectively, are presented in the upper panels of Figure 8 and the best fit virial masses are listed in Table 1. In all cases we see a clear increase of the virial mass with luminosity. The results suggest a power-law relation between the luminosity and the virial mass, although this assumption might not hold at the low luminosity end (e.g., see lower panels of Fig. 8). We therefore fit

$$M = M_{\text{fid}} \left(\frac{L}{10^{10} h^{-2} L_\odot} \right)^\alpha, \quad (10)$$

to the measurements, where M_{fid} is the virial mass of a fiducial galaxy of luminosity $L = 10^{10} h^{-2} L_\odot$, where x indicates the relevant filter. The best fit in each filter is indicated by the dashed line in Figure 8. The resulting

TABLE 2
BEST FIT PARAMETERS OF THE MASS-LUMINOSITY RELATION

filter	M_{fid} [$10^{11} h^{-1} M_\odot$]	α
B	$9.9^{+1.5}_{-1.3}$	1.5 ± 0.3
V	$9.3^{+1.4}_{-1.3}$	1.5 ± 0.2
R	$7.5^{+1.2}_{-1.1}$	1.6 ± 0.2

NOTE. — Column 2 lists the virial mass for a galaxy of luminosity $10^{10} h^{-2} L_\odot$ in the indicated filter. Column 3 lists the best fit power-law slope of the mass-luminosity relation. The listed errors indicate the 68% confidence limits.

best fit parameters for this mass-luminosity relation are listed in Table 2. We do not observe a change in the slope α for the different filter, but find that M_{fid} is decreasing for redder passbands.

Tasitsiomi et al. (2004b) studied the weak lensing mass-luminosity relation from their numerical simulations. This study shows that the interpretation of the mass-luminosity relation presented in Figure 8 is complicated by the fact that the halos of galaxies of a given luminosity show a scatter in their virial masses. For the model adopted in Tasitsiomi et al. (2004b), the best fit virial mass gives a value between the median and mean mass. The amplitude of this bias depends on the assumed intrinsic scatter in the mass-luminosity relation, which requires further study. The Tasitsiomi et al. (2004b) results imply that our results underestimate the actual mean virial mass, but that the slope of the mass-luminosity relation is not changed.

Guzik & Seljak (2002) measured the mass-luminosity relation using data from the SDSS. The average luminosity of their sample of lenses is higher than studied here. Also, the analysis by Guzik & Seljak (2002) differs from ours, as they model the contribution from other halos. Using the halo model approach they compute the contributions of other halos to the lensing signal around a galaxy, including that of smooth group/cluster halos. In this paper, we have instead minimized such contributions to the galaxy-galaxy lensing signal by selecting ‘isolated’ galaxies and limiting the analysis to the lensing signal within $400 h^{-1} \text{kpc}$ from the lens. The results presented in Figures 5 and 6 suggest that this approach has worked well.

Guzik & Seljak (2002) present results for two different cases of group halo contributions. Depending on the assumed relative importance of such a halo the derived

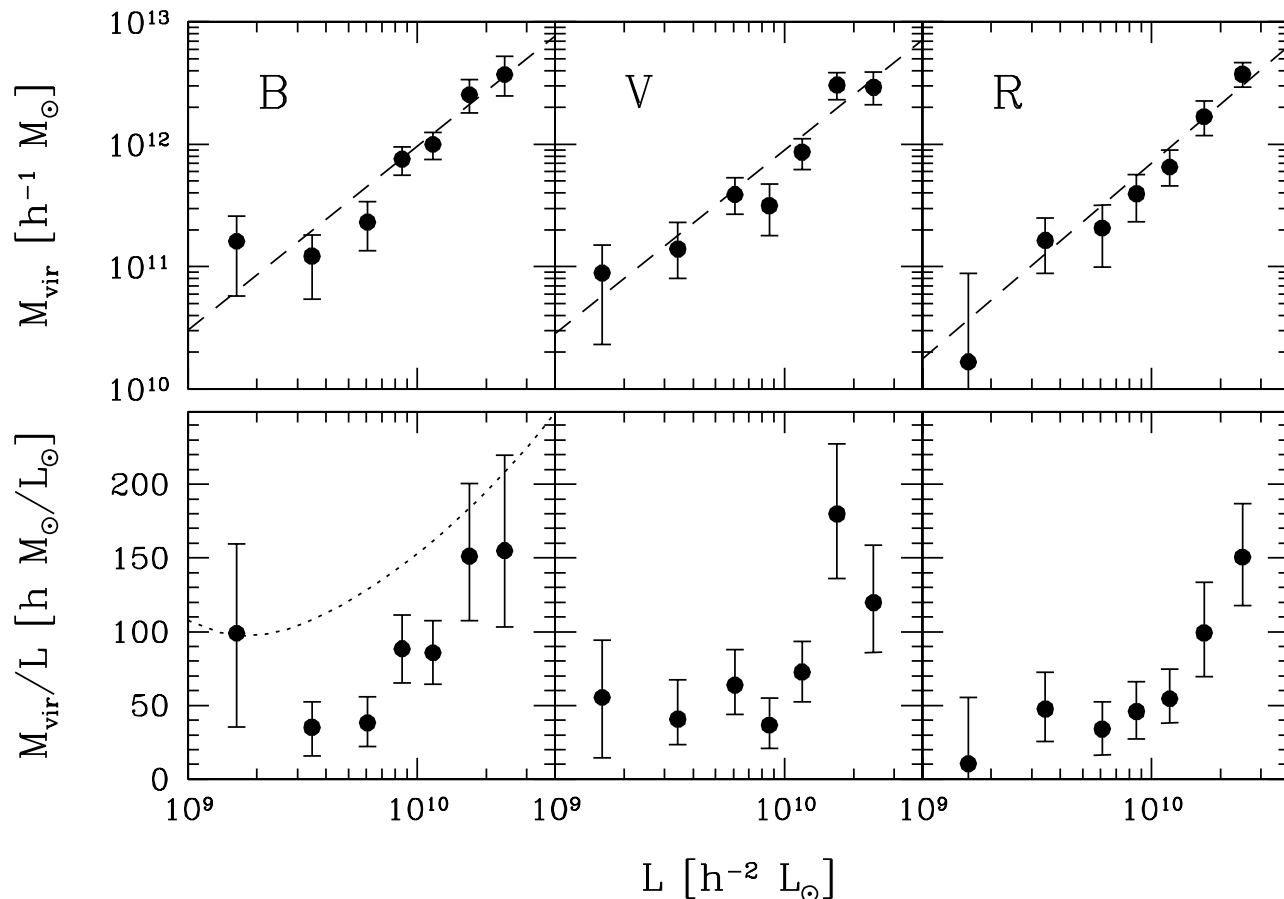


FIG. 8.— *upper panels*: Virial mass as a function of the rest-frame luminosity in the indicated filter. The dashed line indicates the best fit power-law model for the mass-luminosity relation, with the relevant parameters listed in Table 2. *lower panels*: Observed rest-frame virial mass-to-light ratios. The results suggest a rise in the mass-to-light ratio with increasing luminosity, albeit with low significance. The dotted line in the panel showing the *B*-band mass-to-light ratio corresponds to model A from van den Bosch et al. (2003). It matches the observed dependence of the mass-to-light ratio with luminosity, but with an offset towards higher values.

mass changes only slightly. The assumptions for the halo contribution do affect the inferred slopes somewhat, although the change is small for the redder filters. Minimizing the halo contribution yields a power-law slope of $\sim 1.5 - 1.7$, in excellent agreement with the findings presented here. However, when maximizing the effect the slope decreases to $\sim 1.3 - 1.4$ in the red filters and to 1.2 ± 0.2 in the *g'*-band. It should be noted that the latter scenario is rather extreme, given that, with the exception of the central galaxy, the relative importance of the group halo is expected to diminish with increasing luminosity (i.e., mass) of the lens. In addition, the different range in luminosities probed in the two studies would most likely affect the results in the bluest filters.

Benson et al. (2000) present predictions for the *B*-band mass-luminosity relation based on semi-analytic models of galaxy formation. In the luminosity range probed here, they obtain a power-law slope of ~ 1.6 . Van den Bosch et al. (2003) used the conditional luminosity functions computed from the 2dF galaxy redshift survey to constrain the variation of the mass-to-light ratio as a function of mass. Van den Bosch consider a number of models, which provide similar mass-luminosity relations for the range of masses probed in this paper. We consider their model A, which is obtained by fitting the data, without constraining the model parameters. For this

model the mass-luminosity relation is close to a power law with a slope of 1.3. Hence, both model predictions are in good agreement with our findings and the results of Guzik & Seljak (2002).

The agreement in the slope of the mass-luminosity relation strengthens the conclusion by Guzik & Seljak (2002) that rotation curves must decline substantially from the optical to the virial radius, in order to reconcile our results with the observed scaling relations at small radii, such as the Tully-Fisher relation. A decrease in rotation velocity is also predicted by semi-analytic models of galaxy formation (e.g., Kauffmann et al. 1999; Benson et al. 2000).

Guzik & Seljak (2002) define the virial mass in terms of an overdensity of 200 times the critical density, which is different from ours. They find a mass $M_{200} = (9.3 \pm 1.6) \times 10^{11} h^{-1} M_{\odot}$ for a galaxy with a luminosity of $1.1 \times 10^{10} h^{-2} h M_{\odot} / L_{g'_{\odot}}$ at a redshift of $z \sim 0.16$. We convert our mass estimate to their definition, and use the transformations between filters from Fukugita et al. (1996), to relate our results to those of Guzik & Seljak (2002). Furthermore, we assume that the fiducial galaxy is about 10% brighter at $z=0.32$, compared to $z=0.16$. Under these assumptions, our results translate to a mass $M_{200} = (11.7 \pm 1.7) \times 10^{10} h^{-1} M_{\odot}$ for a galaxy with a luminosity of $1.1 \times 10^{10} h^{-2} h M_{\odot} / L_{g'_{\odot}}$, in agreement with

the findings of Guzik & Seljak (2002) at the 1σ level.

The lower panels in Figure 8 show the inferred rest-frame mass-to-light ratios as a function of luminosity for the different filters. The results suggest a rise in mass-to-light ratio for galaxies more luminous than $\sim 10^{10} h^{-2} L_{\odot}$ and little variation for fainter galaxies. This suggests that a power law is not sufficient to describe the mass-luminosity relation over the range probed here. However, a larger data set is needed to make a firm statement. The dashed curve in Figure 8 shows the values corresponding to model A from van den Bosch et al. (2003), converted to the B -band and our definition of the virial mass. The predicted mass-to-light ratio is significantly higher compared to our measurements. This could point to a systematic underestimate of the virial masses from lensing due to scatter in the mass-luminosity relation, as suggested by Tasitsiomi et al. (2004b). Nevertheless, the model predictions are in qualitative agreement with the results presented in Figure 8, in the sense that they predict a rise for bright galaxies and a small increase in mass-to-light ratio towards lower luminosities.

5.2. Star formation efficiency

In the previous section we studied the dependence of the mass-to-light ratio as a function of luminosity. The results suggest an increase for luminous galaxies. A simple interpretation of these results, however, is complicated because the mix of galaxy type is also a function of luminosity. The more luminous galaxies are likely to be early-type galaxies rather than spiral galaxies.

Although we have not classified our sample of lenses, we can use the $B - V$ color as a fair indicator of galaxy type (e.g., Roberts & Haynes 1994). Furthermore, the color can be used to estimate the mean stellar mass-to-light ratio, which also is a strong function of color (e.g., Bell & de Jong 2001). Comparison of the virial and stellar mass-to-light ratios then enables us to estimate the relative fraction of the mass that has been transformed into stars.

Figure 9a shows the inferred B -band mass-to-light ratio as a function of restframe $B - V$ color. Figure 9a shows a clear increase in mass-to-light ratios for early-type galaxies, which have colors redder than ~ 0.8 . It is useful to note that our selection of lenses allows for the brightest galaxies in the centres of denser regions to be included. Our simulations show that the inferred masses are not biased, but these tests do not include the smooth contributions from group halos. The resulting mass-to-light ratios are comparable to those determined for rich clusters of galaxies (e.g., Hoekstra et al. 2002d) and massive galaxy groups (Parker et al. 2005). For galaxies with $B - V < 0.8$ the mass-to-light ratio does not show a clear change with color and we find an average mass-to-light ratio of $M/L_B = 32 \pm 9 h M_{\odot}/L_{B\odot}$. Figure 9b shows the results for the R -band mass-to-light ratio. For galaxies with $B - V < 0.8$ we obtain an average value of $M/L_R = 34 \pm 9 h M_{\odot}/L_{R\odot}$. The increase in mass-to-light ratio for red galaxies is smaller in the R -band, which is expected since the stellar mass-to-light ratios also vary less.

As discussed in the previous section, the measurements presented in Figure 9 are for a sample of galaxies with an average redshift of $z = 0.32$. Note, that to compare these results to measurements at lower redshifts one needs to

account for evolution in both the colors and the luminosities of the lens galaxies. To this end we use population synthesis models (e.g., Fioc & Rocca-Volmerange 1997) which indicate that the galaxies become redder as they age, and that the reddest galaxies dim somewhat faster than the blue galaxies.

As mentioned above, it is interesting to estimate the fraction of mass in stars. To do so, we need to relate the luminosity to the stellar mass. Direct measurements of the stellar mass-to-light ratios are difficult, although rotation curves can provide useful limits on the maximum allowed value. Instead we rely on galaxy evolution models, which use evolutionary tracks and assumptions about initial mass function (IMF), the star formation history and feedback, to compute stellar populations as a function of age.

There are many obvious difficulties in such work, given the complicated history of galaxies and the uncertainty in the IMF. The latter is of particular importance and gives rise to a relatively large uncertainty in the estimates as we will discuss below. Nevertheless, the dependence of stellar mass-to-light ratio with color is fairly well constrained.

Bell & de Jong (2001) used a suite of galaxy evolution models to show that one expects substantial variation in stellar mass-to-light ratio as a function of galaxy color. Although their work focussed on the properties of spiral galaxies, comparison with results for early-type galaxies suggest that we can extend their calculation to these galaxies as well. Bell & de Jong (2001) find the models are well described by a linear relation between $\log M/L$ and $B - V$ color, and provide tables with the slope and intercept of these relations. Their results, however, are for $z = 0$, but we have converted their results to the mean redshift of our lenses ($z = 0.32$) using predictions based on the PEGASE code (Fioc & Rocca-Volmerange 1997), provided by D. LeBorgne. Compared to $z = 0$, the galaxies are slightly bluer, with stellar mass-to-light ratios $\sim 25\%$ lower at $z = 0.32$.

The resulting stellar mass-to-light ratio is most sensitive to the assumed IMF and we will consider two ‘extreme’ cases, such that our results should bracket the real properties of galaxies. The first IMF we consider is the one proposed by Salpeter (1955). The $z = 0.32$ stellar mass-to-light ratios based on the PEGASE code by Fioc & Rocca-Volmerange (1997) are presented in the bottom left panel of Figure 10 for the B (solid line) and R -band (dashed line). As noted by Bell & de Jong (2001) a standard Salpeter (1955) IMF results in mass-to-light ratios that are too high to fit rotation curves of spiral galaxies. Hence, this model can be considered extreme in the sense that it provides a high estimate for the mass in stars. Instead, Bell & de Jong (2001) propose a scaled Salpeter IMF, which is equivalent to reducing the number of low mass stars (which contribute to the mass, but not to the luminosity). We use the parameters from their Table 1. The results for this IMF, which fits the rotation curve data better, are shown in the bottom right panel of Figure 10.

We use these model stellar mass-to-light ratios to calculate the ratio M_{vir}/M_{\star} as a function of color in both B and R band. The results are also presented in Figure 10. For a given model, the results between the two filters agree very well, and the average ratios are listed in

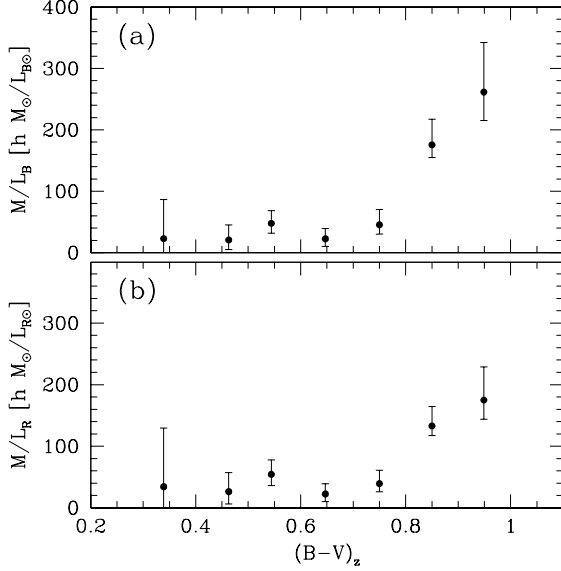


FIG. 9.— (a) Rest-frame B -band virial mass-to-light ratio as a function of rest-frame $(B - V)$ color. (b) The same, but now for the rest-frame R -band. In this case the change for red galaxies is smaller. The filled circles are the measurements for our sample of lenses, which have a mean redshift $z = 0.32$.

Table 3, for a Hubble parameter of $H_0 = 71$ km/s/Mpc. However, the two models yield significantly different ratios.

Observations of the cosmic microwave background (e.g., Spergel et al. 2003) have yielded accurate measurements of the baryon fraction in the universe. Based on WMAP observations, Spergel et al. (2003) obtained $\Omega_b h^2 = 0.024 \pm 0.001$ and $\Omega_m h^2 = 0.14 \pm 0.02$. If we assume that baryons do not escape the dark matter overdensity they are associated with, the ratio of mass in baryons to the total mass of the halo is $M_{\text{bar}}/M_{\text{vir}} = \Omega_b/\Omega_m = 0.17 \pm 0.03$. In the following, we will also assume $H_0 = 71$ km/s/Mpc, which is the currently favoured value.

For the PEGASE Salpeter model, this implies that the fraction of the mass in stars is 0.070 ± 0.011 (average of the B and R value), whereas the scaled Salpeter IMF yields a lower value of 0.037 ± 0.005 . Comparison with the value of Ω_b/Ω_m from CMB measurements suggests that only $\sim 40\%$ and $\sim 22\%$ of the baryons are converted into stars for the standard and scaled Salpeter IMFs respectively. The actual results for the two filters considered here are indicated separately in Table 3 by $f_{\text{bar} \rightarrow *}$.

Table 3 also lists the average results when we consider blue and red galaxies separately. The implied star formation efficiencies for early-type galaxies are low. We note that similar efficiencies have been inferred for galaxy clusters (e.g., Lin, Mohr & Stanford 2003).

Interestingly, our results imply that late-type galaxies convert a ~ 2 times larger fraction of baryons into stars. This result is robust, as it does not depend much on the adopted IMF. Guzik & Seljak (2002) also found a factor of ~ 2 difference in star formation efficiency between early and late-type galaxies, in good agreement with our findings. Hence, these results provide very important, direct observational constraints on the relative star formation efficiency during galaxy formation for different

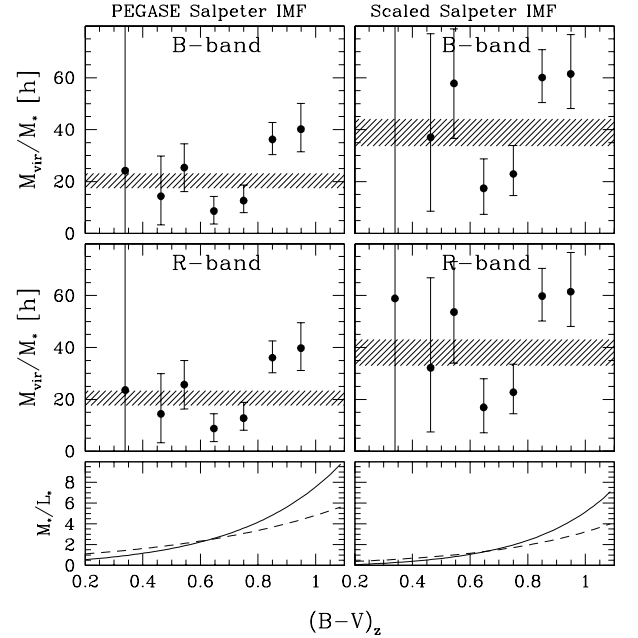


FIG. 10.— Lower panels show the stellar mass-to-light ratios in the B -band (solid lines) and R -band (dashed lines) for the results from PEGASE models using a Salpeter IMF and $Z = 0.02$ (left) and a scaled Salpeter IMF (right) from Table 1 from Bell & de Jong (2001). The mass-to-light ratios have been evolved to $z = 0.32$, which corresponds to the mean redshift of our lens sample. The upper panels show the resulting ratios of virial mass and stellar mass for the B and R -band data. For a given IMF, the results obtained in the different filters agree well, but it is clear that the mean values (indicated by the shaded areas) depend strongly on the adopted IMF.

galaxy types.

These findings suggest that the mechanism for the formation of early type galaxies is somehow more efficient in removing gas compared to late type galaxies. Ram pressure stripping might be more prevalent, given that early type galaxies are typically found in high density regions, or they might form while developing strong winds that blow out most of the baryons.

Irrespective of the process responsible for ejecting baryons, the resulting galaxy will always have a stellar fraction which is greater or equal to the fraction of stars in its progenitors. If we consider the situation where early-type galaxies form through mergers, it is clear that not all early-type galaxies can be the result of merging the late-type galaxies studied in this paper. Ejecting $\sim 60\%$ of the stars during the merger process might seem an option, but this is hard to envision without removing a similar fraction of the dark matter halo.

Hence, the progenitors of early-type galaxies must have had a low fraction of their mass in stars. This could be achieved if early-type galaxies (or their progenitors) formed early on without forming new stars at later times (because they lost their gas) and if later type galaxies sustained their star formation for a much longer time, thus building up a larger fraction of mass in stars. Recent estimates of the star formation rates of high redshift galaxies, suggest a qualitatively similar picture, in which early-type galaxies formed the bulk of their stars very early on with a sharp drop in star formation rates at

TABLE 3
STELLAR MASS AND BARYON FRACTIONS

		PEGASE		SCALED	
		<i>B</i>	<i>R</i>	<i>B</i>	<i>R</i>
all	M_{vir}/M_*	14 ± 2	15 ± 2	27 ± 4	28 ± 4
	$f_{\text{bar} \rightarrow *}$	$0.41^{+0.07}_{-0.05}$	$0.39^{+0.06}_{-0.05}$	$0.22^{+0.04}_{-0.03}$	$0.21^{+0.03}_{-0.03}$
	$f_{\text{bar}}^{\text{gal}}$	$0.070^{+0.012}_{-0.009}$	$0.065^{+0.010}_{-0.008}$	$0.037^{+0.005}_{-0.004}$	$0.035^{+0.005}_{-0.004}$
	f_{bar}				
$B - V < 0.8$	M_{vir}/M_*	9 ± 2	10 ± 3	17 ± 5	18 ± 5
	$f_{\text{bar} \rightarrow *}$	$0.65^{+0.20}_{-0.14}$	$0.60^{+0.20}_{-0.12}$	$0.34^{+0.11}_{-0.08}$	$0.32^{+0.12}_{-0.07}$
	$f_{\text{bar}}^{\text{gal}}$	$0.11^{+0.03}_{-0.02}$	$0.10^{+0.03}_{-0.02}$	$0.057^{+0.018}_{-0.013}$	$0.055^{+0.021}_{-0.011}$
	f_{bar}				
$B - V > 0.8$	M_{vir}/M_*	26 ± 4	28 ± 4	42 ± 6	45 ± 6
	$f_{\text{bar} \rightarrow *}$	$0.22^{+0.03}_{-0.03}$	$0.21^{+0.03}_{-0.03}$	$0.14^{+0.02}_{-0.02}$	$0.13^{+0.02}_{-0.02}$
	$f_{\text{bar}}^{\text{gal}}$	$0.038^{+0.006}_{-0.005}$	$0.036^{+0.005}_{-0.004}$	$0.024^{+0.004}_{-0.003}$	$0.022^{+0.004}_{-0.003}$
	f_{bar}				

NOTE. — Note: Results for the PEGASE model using a standard Salpeter IMF and scaled Salpeter IMF from Bell & de Jong (2001). These models have been evolved to a redshift of $z = 0.32$ to allow for a direct comparison with the measurements. For different color selections, the rows list respectively, the ratio of virial mass over stellar mass, the implied fraction of baryons transformed into stars and the total visible baryon fraction in galaxies. Note that the results for the *B* and *R*-band are not independent. We have adopted a Hubble constant of $H_0 = 71 \text{ km/s/Mpc}$ and a universal baryon fraction of $\Omega_b/\Omega_m = 0.17$ (e.g., Spergel et al. 2003).

$z \sim 2$, and less massive (late-type) galaxies continue to form most of their stars at a later time and over a much longer period of time (e.g., McCarthy et al. 2004; Juneau et al. 2005).

5.3. Visible baryon fraction

In addition to stars, galaxies contain some gas, which needs to be included if we are to do a full accounting of the visible baryon contents of galaxies. Although the amount of molecular hydrogen is uncertain, the amount of neutral hydrogen is relatively well determined from 21cm line studies. The relative amount of HI gas is a function of galaxy type, with late-type galaxies being more gas rich. We use the results from Roberts & Haynes (1994) for the M_{HI}/L_B ratio to estimate the amount of mass in gas (correcting the hydrogen mass to account for the primordial helium abundance). The inclusion of gas slightly raises the mass in detected baryons for the bluest galaxies but this component is negligible for the red galaxies. Adding estimates for the amount of molecular hydrogen does not change the numbers either.

The resulting fraction of the mass in baryons in galaxies, $f_{\text{bar}}^{\text{gal}}$, is listed in Table 3 as well. Only for the blue galaxies, under the assumption of a standard Salpeter (1955) IMF, is the baryon fraction marginally consistent with the value determined from observations of the CMB (Spergel et al. 2003). However, as discussed earlier, the results for this model should be considered upper limits to the baryon fraction, given that the stellar mass-to-light ratios are too high to fit rotation curves (e.g., Bell & de Jong 2001). The results from the Scaled IMF from Bell & de Jong are probably more representative of the actual baryon fractions in galaxies, thus implying that a significant fraction of the gas must have been lost.

6. CONCLUSIONS

We have measured the weak lensing signal as a function of restframe *B*, *V*, and *R*-band luminosity for a sample of ‘isolated’ galaxies, with photometric redshifts $0.2 < z < 0.4$. This selection of relatively isolated galaxies minimizes the contribution of group/cluster halos and nearby bright galaxies.

The photometric redshifts were derived by Hsieh et al. (2005) using $BVR_{CZ'}$ photometry from the Red-Sequence Cluster Survey. To add to the extensive study described in Hsieh et al. (2005), we confronted the photometric redshifts to tests that are unique to weak lensing. These results showed that the lensing signal around a sample of foreground galaxies scales with source redshift as expected. The photometric redshift distribution determined by Hsieh et al. (2005) suggests that the mean redshift of galaxies used in the measurement of the lensing signal by large scale structure (Hoekstra et al. 2002a; 2002b) is somewhat higher than previously assumed. If correct, this would imply a somewhat lower value for the normalization of the matter power spectrum, σ_8 , compared to the published results. The difference is expected to be less than $\sim 10\%$, but with the current data we cannot reliably quantify the size of the change.

Virial masses were determined by fitting an NFW model to the tangential shear profile. Note, that intrinsic scatter in the mass-luminosity relation will result in an underestimate of the mean virial mass for a galaxy of a given luminosity, as suggested by Tasitsiomi et al. (2004b). The magnitude of this effect depends on the assumed scatter, and we have ignored this in our analysis. We found that the virial mass as a function of luminosity is well described by a power-law with a slope of ~ 1.5 , with similar slopes for the three filters considered here. This result agrees with other observational studies (Guzik & Seljak, 2002) and predictions from semi-analytic models of galaxy formation (e.g., Kauffmann et al. 1999; Benson et al. 2000; van den Bosch et al. 2003). For a galaxy with a fiducial luminosity of $10^{10} h^{-2} L_{B\odot}$ we obtained a mass $M_{\text{vir}} = 9.9^{+1.5}_{-1.3} \times 10^{11} M_{\odot}$. Converting this result to match the filter and definition for the mass used by Guzik & Seljak (2002), yields a mass of $M_{200} = (11.7 \pm 1.7) \times 10^{10} h^{-1} M_{\odot}$ for a galaxy with a luminosity of $1.1 \times 10^{10} h^{-2} h M_{\odot}/L_{g'_{\odot}}$, in agreement with Guzik & Seljak (2002), who found $M_{200} = (9.3 \pm 1.6) \times 10^{11} h^{-1} M_{\odot}$.

We examined the efficiency with which baryons are converted into stars. To do so, we used the restframe *B - V* color as a measure of the mean stellar mass-to-

light ratio. The color also provides a crude indicator of galaxy type (e.g., Robert & Haynes 1994). We considered a standard and a scaled Salpeter IMF (see Bell & de Jong 2001). The latter is more realistic, whereas the former yields stellar mass-to-light ratios that are too high to fit rotation curves of spiral galaxies.

Irrespective of the adopted IMF, we found that the stellar mass fraction is about a factor of two lower for early-type galaxies, as compared to late-type galaxies. Including the fraction of baryons in gas only increases the fraction of observed baryons slightly. Hence, our results suggest that galaxy formation is very inefficient in turning baryons into stars and in retaining baryons. These results provide important, direct observational constraints for models of galaxy formation.

Under the assumption that the scaled Salpeter IMF is correct, our results imply that late-type galaxies convert $\sim 33\%$ of baryons into stars. Early-type galaxies do much worse, with an efficiency of $\sim 14\%$. This implies that the progenitors of early-type galaxies have a low fraction of their mass in stars. A possible explanation of this result is that early-type galaxies formed early on and stopped forming new stars, because they lost most of their baryons (e.g., through winds or ram pressure stripping). If later type galaxies, on the other hand, continued to form stars this would lead to a higher stellar mass fraction. Such a scenario is, at least qualitatively, in agreement with recent estimates of the star formation rates of high redshift galaxies (e.g., McCarthy et al. 2004; Juneau et al. 2005).

REFERENCES

- Bartelmann, M. 1996, *A&A*, 313, 697
 Bell, E.F. & de Jong, R.S. 2001, *ApJ*, 550, 212
 Benson, A.J., Cole, S., Frenk, C.S., Baugh, C.M., & Lacey, C.G. 2000, *MNRAS*, 311, 793
 Bernstein, G.M. & Norberg, P. 2002, *AJ*, 124, 733
 Bryan, G.L. & Norman, M.L. 1998, *ApJ*, 495, 80
 Bullock, J.S. et al. 2001, *MNRAS*, 321, 559
 Capak, P. et al. 2004, *AJ*, 127, 180
 Connolly, A.J., Csabai, I. & Szalay, A.S. 1995, *AJ*, 110, 2655
 Cowie, L.L., Barger, A.J., Hu, E.M., Capak, P., & Songaila, A. 2004, *AJ*, 127, 3137
 Diemand, J., Moore, B. & Stadel, J. 2004, *MNRAS*, 353, 624
 Dubinski, J. & Carlberg, R.G. 1991, *ApJ*, 378, 496
 Faber, S.M. & Jackson, R.E. 1976, *ApJ*, 204, 668
 Fioc, M. & Rocca-Volmerange, B. 1997, *A&A*, 326, 950
 Fischer, P., et al. 2000, *AJ*, 120, 1198
 Fukugita, M., Ichikawa, T., Gunn, J.E., Doi, M., Shimasaku, K., & Schneider, D.P. 1996, *AJ*, 111, 1748
 Gladders, M.D. & Yee, H.K.C. 2005, *ApJS*, 157, 1
 Guzik, J., & Seljak, U. 2001, *MNRAS*, 321, 439
 Guzik, J., & Seljak, U. 2002, *MNRAS*, 335, 311
 Hayashi, E., Navarro, J.F., Power, C., Jenkins, A., Frenk, C.S., White, S.D.M., Springel, V., Stadel, J., & Quinn, T.R. 2004, *MNRAS*, 355, 794
 Hoekstra, H., Yee, H.K.C., Gladders, M.D., Barrientos, L.F., Hall, P.B., & Infante, L. 2002a, *ApJ*, 572, 55
 Hoekstra, H., Yee, H.K.C., & Gladders, M.D. 2002b, *ApJ*, 577, 595
 Hoekstra, H., van Waerbeke, L., Gladders, M.D., Mellier, Y., & Yee, H.K.C. 2002c, *ApJ*, 577, 604
 Hoekstra, H., Franx, M., Kuijken, K. & van Dokkum, P.G. 2002d, *MNRAS*, 333, 911
 Hoekstra, H., Yee, H.K.C., & Gladders, M.D. 2004, *ApJ*, 606, 67
 Hsieh, B.C., Yee, H.K.C., Lin, H., & Gladders, M.D. 2005, *ApJS*, in press
 Hudson, M.J., Gwyn, S.D.J., Dahle, H., & Kaiser, N. 1998, *ApJ*, 503, 531
 Juneau, S. et al. 2005, *ApJ*, 619, L135
 Kauffmann, G., Colberg, J.M., Diaferio, A., White, S.D.M. 1999, *MNRAS*, 303, 188
 Keeton, C.R., Kochanek, C.S., & Falco, E.E. 1998, *ApJ*, 509, 561
 Lin, H., Yee, H.K.C., Carlberg, R.G., Morris, S.L., Sawicki, M., Patton, D.R., Wirth, G. & Shepherd, C.W. 1999, *ApJ*, 518, 533
 Lin, Y.-T., Mohr, J.J., & Stanford, S.A. 2003, *ApJ*, 591, 749
 McCarthy, P.J. et al. 2004, *ApJ*, 614, L9
 McKay, T.A., et al. 2001, *ApJ*, submitted, astro-ph/0108013
 Moore, B., Quinn, T., Governato, F., Stadel, J., & Lake, G. 1999, *MNRAS*, 310, 1147
 Navarro, J.F., Frenk, C.S., & White, S.D.M. 1995, *MNRAS*, 275, 56
 Navarro, J.F., Frenk, C.S., & White, S.D.M. 1996, *ApJ*, 462, 563
 Navarro, J.F., Frenk, C.S., & White, S.D.M. 1997, *ApJ*, 490, 493
 Parker, L.C., Hudson, M.J., Carlberg, R.G., & Hoekstra, H. 2005, *ApJ*, submitted
 Roberts, M.S., & Haynes, M.P. 1994, *ARA&A*, 32, 115
 Salpeter, E.E. 1955, *ApJ*, 121, 61
 Sheldon, E.S., et al. 2004, *AJ*, 127, 2544
 Smith, D.R., Bernstein, G.M., Fischer, P., & Jarvis, M. 2001, *ApJ*, 551, 643
 Spergel, D.N. et al. 2003, *ApJS*, 148, 175
 Tasitsiomi, A., Kravtsov, A.V., Gottlöber, S. & Klypin, A.A. 2004a, *ApJ*, 607, 125
 Tasitsiomi, A., Kravtsov, A.V., Wechsler, R.H. & Primack, J.R. 2004b, *ApJ*, 614, 533
 Tully, R.B. & Fisher, J.R. 1977, *A&A*, 54, 661
 van Albada, T.S., & Sancisi, R. 1986, *Phil. Trans. Roy. Soc., London*, A320, 447
 van den Bosch, F., Yang, X., & Mo, H.J. 2003, *MNRAS*, 340, 771
 van Dokkum, P.G., & Franx, M. 1996, *MNRAS*, 281, 985
 Verheijen, M.A.W. 2001, *ApJ*, 563, 694
 Wilson, G., Kaiser, N., Luppino, G.A., Cowie, L.L. 2001, *ApJ*, 555, 572
 Wirth, G.D. et al. 2004, *AJ*, 127, 3121
 Wright, C.O. & Brainerd, T.G. 2000, *ApJ*, 534, 34
 Yee, H.K.C. et al. 2000, *ApJS*, 129, 475